ORIGINAL ARTICLE

Hot working behaviour of low-cost Ti-3.4Fe bio-implant alloy

Dineo Mosoma[1] · Desmond Klenam[1] · Takunda Maunganidze[1,2] · Michael Bodunrin[1,3]

Abstract

This study investigated the hot workability of an experimental, non-toxic, low-cost Ti-3.4Fe alloy using flow stress analysis, constitutive modelling, processing maps and microstructural examination. Hot compression tests were performed on Ti-3.4Fe alloy samples at different deformation temperatures (750, 800, 850 and 900 °C), strain rates (0.05, 0.1, 1 and 10 s^{-1}) and a total strain of 0.6. The compression tests were performed using a Gleeble® 3500 thermomechanical simulator. The isothermally compressed samples were analysed using a scanning electron microscope to assess the microstructure. An Arrhenius-based model was used to derive the constitutive constants. From the results, the stress exponent and activation energy were 4.91 and 611 kJ.mol^{-1} under the steady-state stress condition and 5.32 and 675 kJ.mol^{-1} at peak stress. The stress exponents suggested a dislocation climb and glide mechanism controlling deformation. The processing map showed that the optimum conditions to deform Ti-3.4Fe were 850 °C at a strain rate of 0.1 s^{-1} for both steady-state and peak stresses. The microstructure revealed kinked, rotated and bent lamella at the safe region (850 °C at 0.05 s^{-1}), confirming the dominance of dynamic recovery as the softening mechanism. Instabilities manifested as cracks and inhomogeneity at 750 °C and 1 s^{-1} and at 850 °C and 10 s^{-1}.

Keywords Processing maps · Hot deformation · Constitutive analysis · Microstructural evolution · Dynamic recovery

1 Introduction

Titanium and its alloys have excellent mechanical properties, biocompatibility, and corrosion resistance. These properties make them desirable in many applications, including aerospace, automotive and biomedical industries [1]. Like other metallic materials, the properties of titanium alloys are mainly influenced by their microstructure [2]. This makes it important to control the microstructure of titanium alloys during processing through heat treatment or thermomechanical means. Titanium alloys can be classified based on the dominant phase constituents in their microstructure. The

near α and the near β alloys are additional subclasses of the three main groups of titanium alloys (α, α + β, and β phases) [3, 4].

The biomedical industry has considered every type of titanium alloy; however, commercially pure titanium and Ti-6Al-4 V, an α + β type alloy, have been used the most [5]. Due to complications caused by Al and V in Ti-6Al-4 V when inserted into the body as an implant, the use of non-toxic alloying components like Zr, Nb, Ta, and Mo has been investigated. Complications associated with the Ti-6Al-4 V include a build-up of osteointegration leading to peri-implantitis, and the alloying element Al has been associated with neurotoxicity and senile dementia [6, 7]. Dörner et al. [8] reported a case of inflammatory arthritis observed after receiving a Ti-6Al-4 V implant [8]. Despite these interventions, Ti-6Al-4 V still dominates in the bioimplant industry because it is slightly cheaper than many biomedical grade β-Ti alloys. The beta titanium alloys offer lower elastic modulus than other Ti alloys, but the alloying elements like Ta, Mo and Nb are highly priced.

To address the high cost and toxicity challenge, Fe, the cheapest beta-stabilising element and a eutectoid former [9], was considered the sole alloying element in developing a

✉ Michael Bodunrin
Michael.Bodunrin@wits.ac.za

1 School of Chemical and Metallurgical Engineering, DSI-NRF Centre of Excellence in Strong Materials, University of the Witwatersrand, Private Bag 3, WITS, Johannesburg 2050, South Africa

2 School of Mechanical, Industrial and Aeronautical Engineering, University of the Witwatersrand, Private Bag 3, WITS, Johannesburg 2050, South Africa

3 African Academy of Sciences, P.O. Box 24916-00502, Nairobi, Kenya

biomedical grade Ti-3.4Fe alloy in this study. Leshetla et al. [10] demonstrated that Ti-3.4Fe's corrosion rate was far lower than 0.50 mm/yr in simulated body fluids. The corrosion rate of this alloy was also lower than the recommended maximum corrosion rate of 0.13 mm/yr for the design of biomedical alloys [11]. To the best of the authors' knowledge, this alloy's hot deformation behaviour has not been explored previously. Furthermore, it is envisaged that this alloy will not be used in the as-cast condition; rather, it will be formed into different shapes and sizes depending on the type of biomedical components to be manufactured. The hot working of alloys influences the evolution of new microstructure and processing parameters, like temperature, strain, and strain rate, affecting their deformation behaviour [12]. This study aimed to establish the most advantageous processing conditions for forming Ti-3.4Fe alloy into different shapes. These optimum processing conditions would help save processing time and cost during large-scale industrial production. In addition, reproducible microstructure and dominant deformation mechanisms were established using flow stress analysis, constitutive modelling, and processing maps with microstructural validation.

Constitutive analysis predicts the flow stress, and processing maps are useful in determining the optimum deformation conditions and dominant softening mechanisms of deformed alloys. For Ti alloys, the flow stress is sensitive to small changes in the deformation parameters, including deformation temperature, strain rate, and strain [13]. Also, compositional variation and initial microstructure influence the response of Ti alloys to imposed deformation parameters. Thus, Ti alloys reportedly have a narrow processing window compared to steel and aluminium [13, 14]. Researchers have taken advantage of this knowledge to tailor the deformation of Ti alloys and investigate the link between hot working parameters, microstructural evolution, and mechanical properties [15].

Hot deformation exhibits several softening mechanisms, such as dynamic recovery, dynamic recrystallisation, dynamic globularisation, superplasticity and flow localisation [15, 16]. Amongst these, dynamic recovery, dynamic recrystallisation, dynamic globularisation, and superplasticity are desirable, while flow localisation, wedge cracking, incipient melting, and adiabatic shear banding are considered unsafe [15, 16]. In this study, the hot deformation behaviour of the as-cast experimental Ti-3.4Fe alloy was evaluated. The alloys were produced using a vacuum induction melting furnace — details are presented elsewhere [10]. It is envisaged that the findings from this work would provide additional information on low-cost experimental titanium alloys that are potentially designed for biomedical applications.

2 Materials and methods

2.1 Casting Ti-3.4Fe alloy

Commercially pure titanium and iron rods with 99.99% purity were melted using a vacuum induction melting furnace after weighing. The total charge was approximately 4 kg and melting was carried out in an yttria crucible. The molten alloy was poured into a steel mould and allowed to solidify. Thereafter, the alloy was fettled and sectioned for chemical analysis using optical emission and energy-dispersive x-ray spectroscopy. The alloy's average chemical composition obtained from both techniques is presented in Table 1. The iron content obtained from both types of spectroscopy was similar, but the energy-dispersive x-ray did not pick up oxygen and nitrogen. Traces of yttrium were picked in both techniques.

2.2 Isothermal compression testing

Ti-3.4Fe alloy samples were isothermally compressed on the Gleeble® 3500 thermomechanical simulator. The initial microstructure of the Ti-3.4Fe alloy (Fig. 1) shows a thick lamellar microstructure. There are also some yttrium impurities in the alloy from casting, observed as bright white spots. The samples were machined into 12 mm length and 8 mm diameter spherical samples. Before deformation, the samples were heated directly to
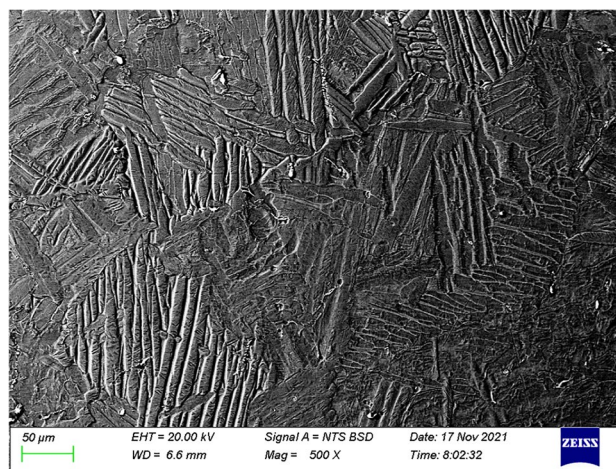

Fig. 1 Initial microstructure with fully lamellar structure

Table 1 Ti-3.4Fe alloy's average chemical composition

Element	Titanium	Iron	Oxygen	Nitrogen	Yttrium
Weight (%)	96.33 ± 0.06000	3.40 ± 0.02000	0.21 ± 0.00020	0.009 ± 0.00300	0.05 ± 0.00001

between 750 and 900 °C and soaked for 180 s to homogenise. The deformation was carried out at different strain rates of 0.05, 0.1, 1, and 10 s^{-1} at every deformation temperature to a total strain of 0.6. The deformation parameters selected in this work are consistent with those explored in other studies [15–20], and as such, the results obtained from this work can be compared with those reported previously on the hot working of titanium alloys [17, 18]. Additionally, the parameters selected in this work fall within the range of parameters used for forging, rolling, extrusion and sheet metal forming in a typical metal processing plant [19, 20]. The stress–strain data collected from the Gleeble® software were then used for constitutive analysis and building processing maps following the test. These are discussed in the subsequent sections.

2.3 Constitutive modelling

The peak flow stress and stress at final strain (taken as the steady-state stress) obtained from isothermal compression testing were used to find the constitutive constants. A hyperbolic sine equation (Eq. (1)) that is derived using the Arrhenius equation modified with the incorporation of the Zener-Hollomon parameter (Z) was used to calculate the apparent activation energy and stress exponents [21–23]. The equations are described as follows:

$$\dot{\varepsilon} = A[\sin h(\alpha\sigma)]^n \exp\left(-\frac{Q}{RT}\right) for all \sigma \tag{1}$$

$$Z = \dot{\varepsilon}\exp(\frac{Q}{RT}) \tag{2}$$

A, m, n, α, and β are constants, and R, T, Q, and ἐ are the universal gas constant, absolute temperature, activation energy, and strain rate, respectively. The equation predicts flow stress and suggests possible softening mechanisms that control deformation using Q and n. Predicted stress can be calculated using Eq. (3). The predictability of the model can be determined using the root-mean-square error (RMSE) and average absolute relative error (AARE) calculated using Eqs. (4) and (5) [3].

$$\sigma = \frac{1}{\alpha}\{\left(\frac{Z}{A}\right)^{\frac{1}{n}} + [\left(\frac{Z}{A}\right)^{\frac{2}{n}} + 1]^{\frac{1}{2}}\} \tag{3}$$

$$RMSE = \frac{1}{N}\sum_{i=1}^{N}\left|\frac{\sigma_i - P_i}{\sigma_i}\right| \tag{4}$$

$$AARE = \sqrt{\frac{1}{N}\sum_{i=1}^{N}(\sigma_i - P_i)^2} \tag{5}$$

2.4 Processing map development

Using the Prasad and Seshacharyulu [24] technique, the processing maps were created by superimposing the instability map with the power dissipation efficiency map. The power dissipation efficiency map values were determined using Eq. (5), where m is the strain rate sensitivity parameter described by Eq. (6).

$$\eta = \frac{2m}{(m+1)} \tag{6}$$

$$m = \frac{\partial ln\sigma}{\partial ln\dot{\varepsilon}} \tag{7}$$

The values for the instability map were determined using Eq. (7), which describes Murty's instability criterion. It is similar to that of Prasad and Seshacharyulu, such that it shows unstable flow at high strains; however, it exhibits a narrower unstable region compared to Prasad and Seshacharyulu's instability criterion [25]. Murty's criterion (Eq. (8)) assumes that m is a variable, and it is used to predict more accurate instability regions compared to Prasad's because of its strict calculations and inferences [25].

$$\zeta\dot{\varepsilon} = \frac{2m}{\eta} - 1 < 0 \tag{8}$$

The instability map predicts the unstable deformation regions of different metallic alloys [26]. The instability map was developed at both the peak stress and the steady-state flow stress. The peak flow stress varies with temperature and strain rate as described by the Zener-Hollomon parameter, and the steady-state flow stress is used to make the Zener-Hollomon parameter independent of strain [27, 28].

2.5 Microstructural examination

The deformed samples were sectioned in half parallel to the compression axis. The sectioned samples were mounted, polished, ground, and etched using Kroll's Reagent. The samples were then examined under a scanning electron microscope. The images of the microstructures of the deformed Ti-3.4Fe alloy samples obtained were compared with the initial microstructure to establish the microstructural evolution and dominant deformation mechanisms.

3 Results and discussion

3.1 Flow stress analysis

Figure 2 shows the stress–strain graphs constructed from the hot compression of the Ti-3.4Fe alloy. The flow curves show that flow stress increased with increasing strain rates and decreased with increasing temperature. Increasing the strain rate increased the mobile dislocation speed and flow stress [21]. Longer energy accumulation and greater dynamic softening brought on by a high temperature aid in removing dislocation entanglement [2, 29]. The flow stress rapidly increased until the maximum peak stress was reached at a very low strain (0 to 0.05). This is due to work hardening [2]. For most of these curves, steady-state stress was reached after peak stress due to the counterbalancing of work hardening and flow softening. However, in cases where the flow stress dropped continuously after attaining the maximum stress, flow softening exceeded work hardening [30, 31]. For all curves at all strain rates, work hardening was observed at very low strain; some reached peak stress and continued at nearly steady-state stress, such as all the 900 °C curves for all strain rates. After peak stress was reached for 850 °C at 0.05 s^{-1} and 800 °C at 1 s^{-1}, the flow stress decreased gradually until steady-state flow stress was obtained. The shape of the curves suggests a possible softening mechanism that controls the deformation of

metallic alloys [2]. The flow stress curves in Fig. 2 show work hardening at low strain. The flow stress curves conformed to the conventional dynamic recovery characteristics for the vast majority of the curves, except 850 °C at 0.05 s^{-1} and 800 °C at 1 s^{-1}. The flow curves can only suggest a softening mechanism controlling deformation in the hot working of the alloy; further analysis is needed to validate these suggestive mechanisms.

3.2 Constitutive modelling

3.2.1 Material constants

The apparent activation energy and stress exponent can be used to propose the mechanism controlling deformation [3, 26]. Figures 3 and 4 show fitting lines for the constitutive constants. The average of the slopes from the plot of lnέ vs σ and lnέ vs lnσ for the different deformation temperatures was used to determine the values for β and ṅ. Then, α was calculated using β/ṅ. The fitting line for lnέ vs ln[sinh(ασ)] was used to find n while the ln[sinh(ασ)] vs 1000/T fitting line determined K. From these values, the activation energy was calculated using Eq. (9).

$$Q = RlnK \tag{9}$$

where R is equal to 8.314 J/mol.K. Equation (10) was used to find A. The lnZ vs nln[sinh(ασ)] fitting line was used to

Fig. 2 Flow curves of the Ti-3.4Fe alloy at different strain rates (**a**) 0.05 s^{-1}, (**b**) 0.1 s^{-1}, (**c**) 1 s^{-1}, and (**d**) 10 s.$^{-1}$
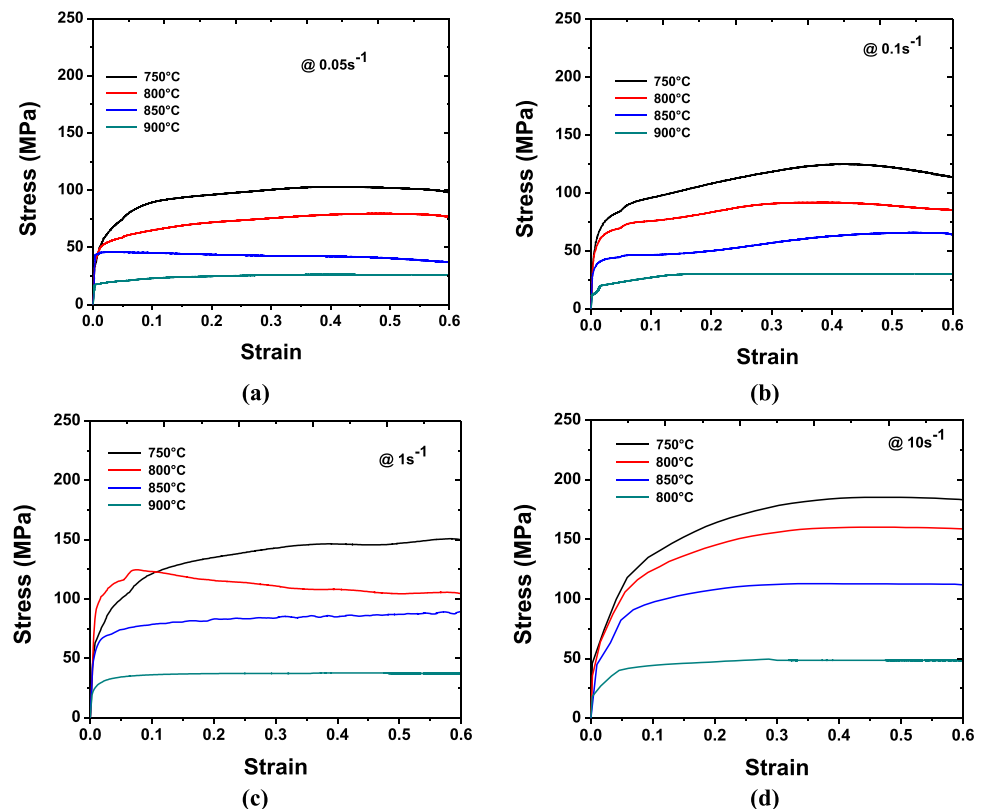
Fig. 3 Determination of constitutive constants at peak stress for Ti-3.4Fe alloy (**a**) β, (**b**) $\dot{n}$, (**c**) n, (**d**) k, and (**e**) ln$A$

(a)

(b)

(c)

(d)

(e)
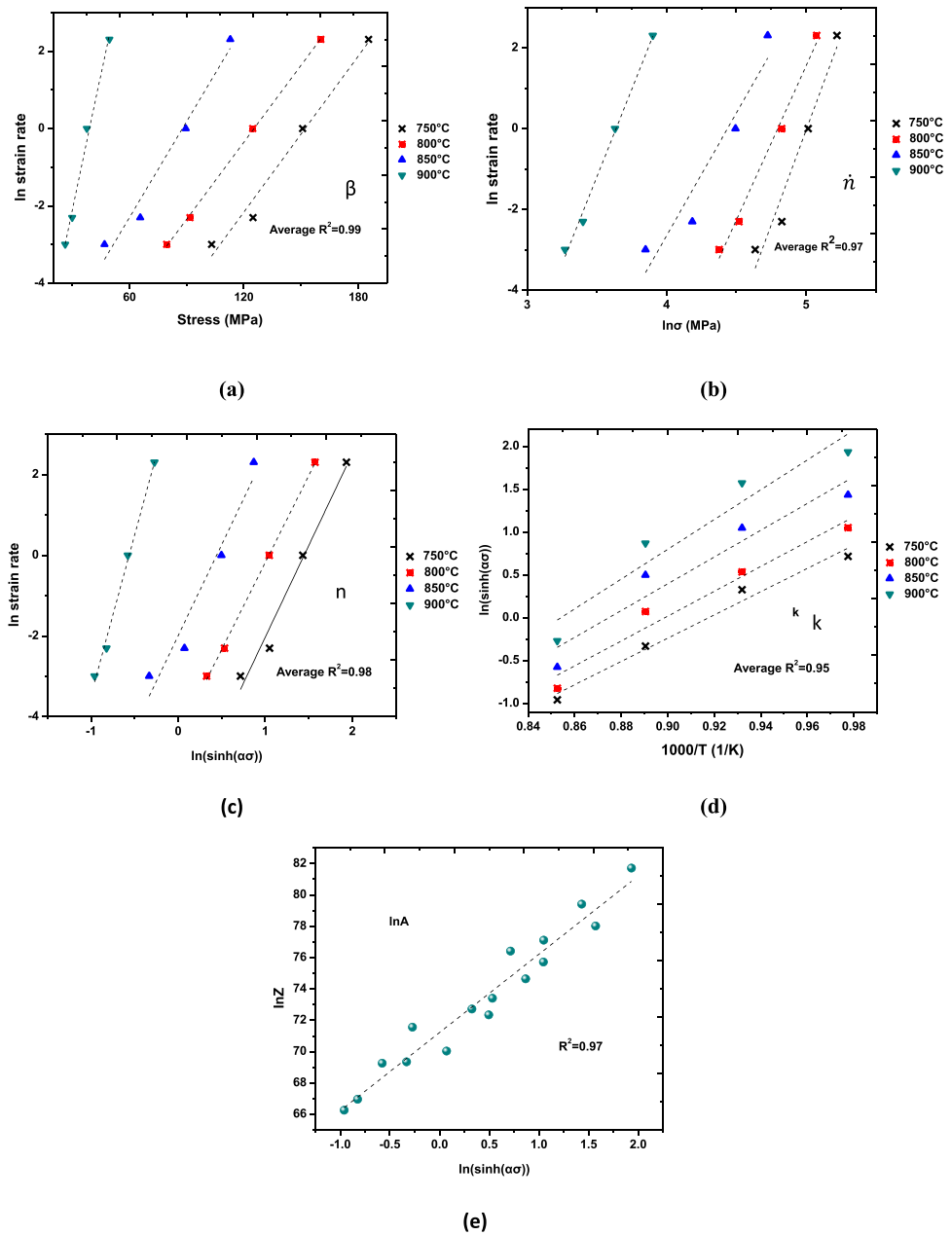
optimise Z, as can be seen in Figs. 3 and 4, where ln$A$ was found using Eq. (1).

$$lnZ = lnA + nln[\sinh(\alpha\sigma)] \quad (10)$$

The constants change with changing strain due to microstructural evolution during hot deformation [3]. When the steady-state stress values were used, the activation energy for hot working decreased to 611 kJ.mol^{-1} from its initial value of 675 kJ.mol^{-1} when it was determined using the peak stress. The stress exponents were 5.32 and 4.91 for peak stress and steady-state stress, respectively (Table 2). The glide and climb of dislocations are what control deformation at high temperatures, and the stress exponent is typically calculated as being ~ 5 [32, 33]. From this work, the stress exponents at peak stress and steady-state stress were both near 5, suggesting that dislocation climb and glide is the main mechanism controlling hot deformation. Dislocation climb and glide is typically observed for dynamic recovery, which occurs when the flow stress reaches a stable condition after the peak stress has been attained [2]. This agrees with the trends observed in Fig. 2, where most of the flow curves showed typical dynamic recovery behaviour. The apparent activation energies, 675 kJ.mol^{-1} and 611 kJ.mol^{-1}, are significantly

Fig. 4 Determination of constitutive constants at steady-state stress for Ti-3.4Fe alloy (**a**) β, (**b**) $\dot{n}$, (**c**) n, (**d**) K, and (**e**) ln$A$
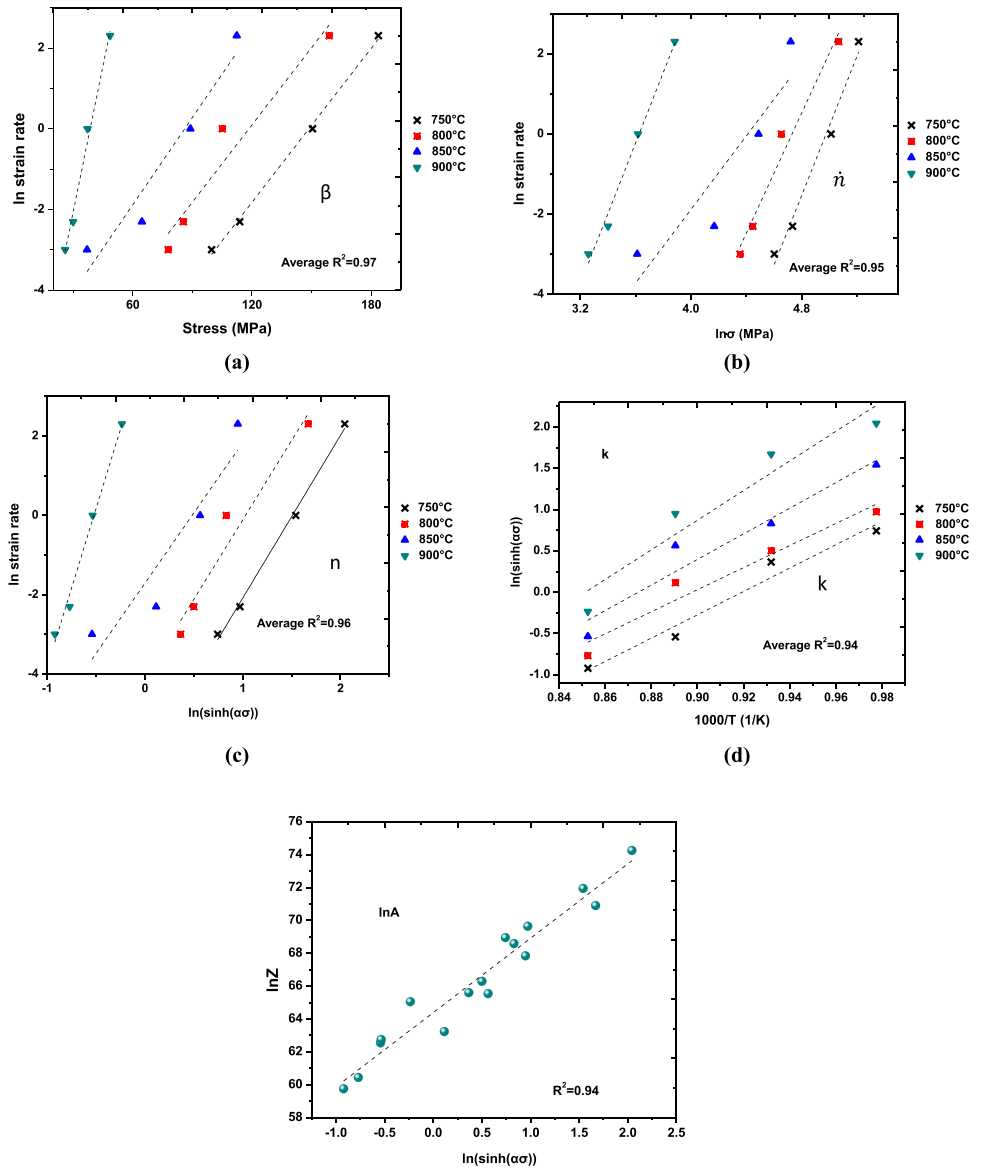
Table 2 Constitutive constants at peak stress and steady-state stress for hot working Ti-3.4Fe experimental alloy

	β	$\dot{n}$	A (MPa^{-1})	n	K	Q (kJ.mol^{-1})	A (s^{-1})
Peak stress	0.11	7.93	0.0142	5.32	15.26	675.41	8.52×10^{30}
Steady-state stress	0.11	7.38	0.0149	4.91	14.98	611.90	9.27×10^{27}

higher than the self-diffusion activation energy of $\alpha + \beta$-Ti (156 kJ.mol^{-1}), α-Ti (150 kJ.mol^{-1}) and β-Ti (153 kJ.mol^{-1}) [34, 35] but are within the values reported by previous authors on hot worked titanium alloys [21, 22]. Dynamic recovery requires the self-diffusion activation to be equal to or nearly equal to the apparent activation energy [27]. High activation energies, typically 300 to 700 kJ.mol^{-1}, are usually associated with dynamic recrystallisation as the predominant softening mechanism [2, 28]. However,

because the apparent activation energy for the hot working of this alloy was determined using an Arrhenius phenomenological model, the activation energy has no physical meaning and, as such, cannot be used to make conclusive remarks on the dominant softening mechanisms during deformation [36]. Processing maps and microstructural evolution can establish the various softening mechanisms during the deformation of Ti-3.4Fe. This is presented in Sect. 3.3.

3.2.2 Predictability of the constitutive models

The predictability of the constitutive model was determined using the correlation coefficient (R^2), RMSE, and AARE. For Ti-3.4Fe, the R^2, RMSE and AARE were 95%, 11.2%, and 10.7% at peak stress, and 92%, 13.6%, and 15.5% at steady-state stress (0.6 strain) (Fig. 5). The AARE and RMSE are relatively low for both peak and steady-state stress constitutive modelling; they fall within the range reported in previous studies of titanium alloys [21, 22]. The model developed using the peak stress values had a higher correlation coefficient and lower RMSE and AARE than the model derived from steady-state stress. This allows for a more accurate estimate of flow stress using the peak stress values for this alloy [27]. The correlation coefficient, RMSE, and AARE can be further enhanced using an artificial neural network or generalised reduced gradient approach, as reported by previous authors [21, 22, 37].

3.3 Processing map and microstructural evolution

3.3.1 Processing map developed using the peak stress

The power dissipation and instability maps (Fig. 6) show the mechanism controlling deformation at different hot working conditions, helping to identify which regions to avoid when carrying out hot working [38]. The region of instability should be avoided during hot working. The power dissipation efficiency ranged from 12 to 68% with the largest region having a power dissipation efficiency of less than 30% (Fig. 6a). When $\eta < 30$, dynamic recovery is the dominant softening mechanism controlling deformation [39]. Dynamic recovery occurs through cross-slip for high stacking fault energy (SFE) metals and occurs by climb in low stacking fault metals [40]. Pure titanium is typically softened by dynamic recovery due to it being a high stacking fault energy metal [41]. The SFE (γ_{SFE}) of pure titanium

Fig. 5 Error calculation at (**a**) peak stress and (**b**) steady-state stress
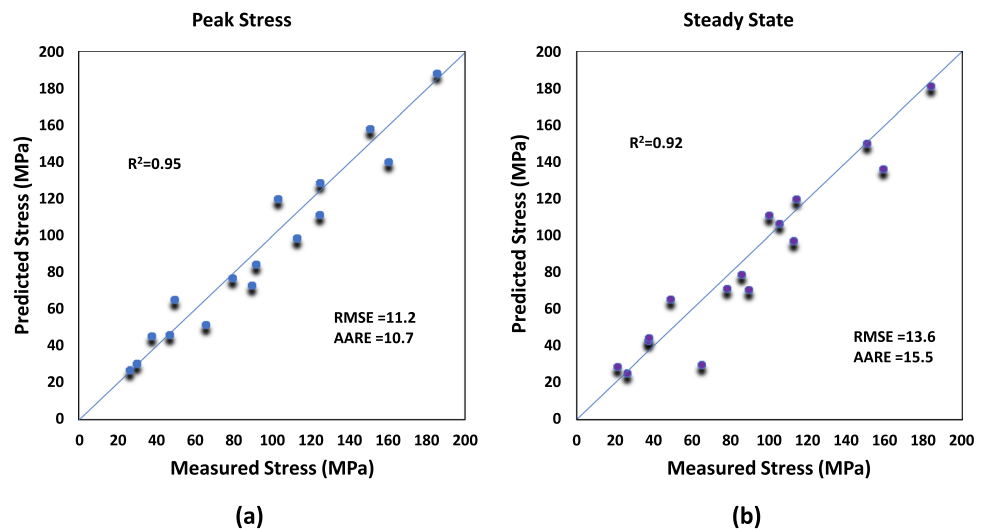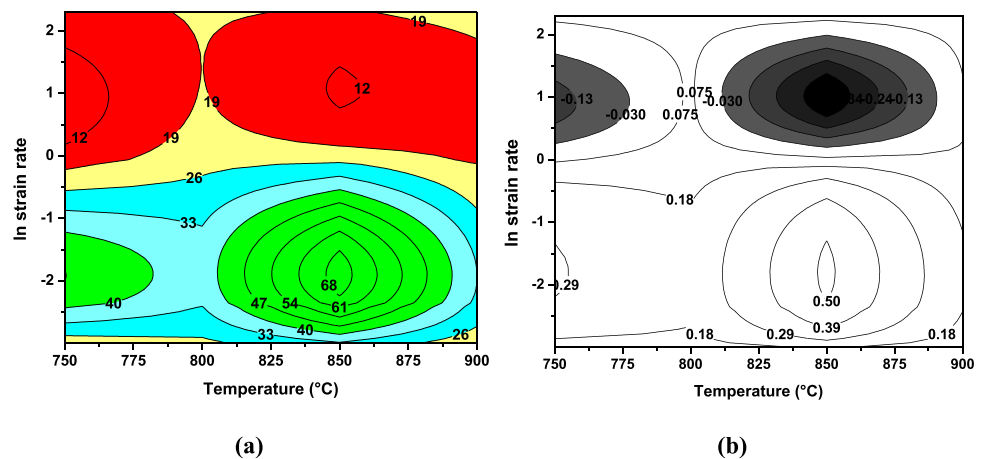
Fig. 6 Ti-3.4Fe alloy (**a**) power dissipation map and (**b**) instability map at peak stress

has been reported to be in the range of 0.3 to 0.35 J/m^2, but aluminium has been reported to characteristically decrease the SFE in titanium alloys containing different concentrations of Al (N_{Al}) following the relation $\gamma_{SFE} = 0.00093/[0.003\exp(0.133N_{Al})]$ [42]. The Ti-3.4Fe alloy considered in this study does not contain Al, so it is expected that the SFE will fall within the range of 0.30 to 0.35 J/m^2, which will favour softening by dynamic recovery. The power dissipation map (Fig. 6(a)) shows that the alloy is primarily softened by dynamic recovery. However, a high-power dissipation efficiency of 68% was obtained at the optimum region, indicating the occurrence of superplasticity. Although Fe has been reported to promote superplasticity in titanium due to its fast diffusion in titanium [43], this behaviour was not confirmed experimentally in this study; it will be considered in a future work. An instability region was found between 1 and 10 s^{-1} at temperatures between 810 and 885 °C and

750 and 780 °C (Fig. 6(b)). Hot working at this region would produce defects such as cracking in the microstructure.

The processing map shows that the optimum region of Ti-3.4Fe is at 850 °C and 0.1 s^{-1}, which is marked X in the area displayed in Fig. 7. This region has the highest power dissipation of 68%, indicating a dominant softening mechanism of superplasticity. Microstructural evidence at the peak stress and corresponding strain will be required to affirm the softening mechanism. The processing map shows a wide processing window for the conditions tested. The largest region of the processing map has a power dissipation of less than 30 ($\eta < 30$), which can be attributed to dynamic recovery, agreeing with the flow curves and constitutive modelling that suggested that dynamic recovery is the dominant softening mechanism. The processing map was not validated at peak stress because the total strain of 0.6 was used.

3.3.2 Processing map developed using the steady-state stress

At steady-state stress, the instability region was determined to be between 1 and 10 s^{-1} at temperatures between 800 and 900 °C (Fig. 8). As in the peak stress, this region at the steady-state stress should be avoided when hot working. The power dissipation efficiency ranges from 10 to 90% with the largest region having a power dissipation of less than 30 ($\eta < 30$). This further supports the conclusion that the dominant mechanism controlling deformation is dynamic recovery, as seen in the peak stress processing map.

The processing map also shows a broad processing window within the tested deformation temperature and strain rates at a strain of 0.6 (Fig. 9). The optimum conditions to deform the alloy was determined to be at 0.1 s^{-1} and 850 °C. This region has the highest power dissipation efficiency of 90%. When $\eta > 60\%$, the suggested mechanism controlling hot deformation is superplasticity [44]; however, this was not confirmed experimentally in this study. Superplasticity ordinarily occurs at low strain rates ($\sim 10^{-3}$) and microstructural
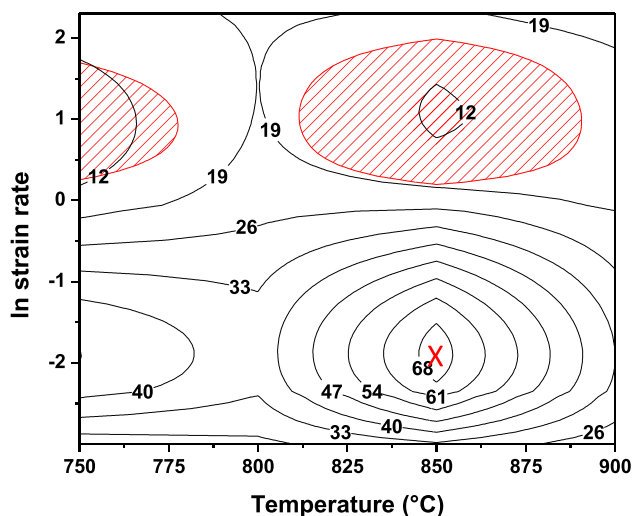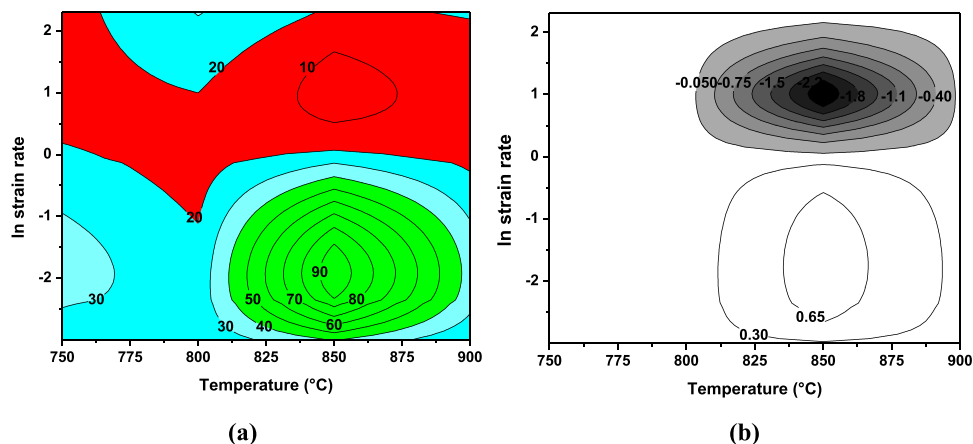

Fig. 7 Processing map of Ti-3.4Fe alloy at peak stress; the shaded area shows the instability region, and the region marked with X shows the optimum region to deform

Fig. 8 Ti-3.4Fe alloy (**a**) power dissipation map and (**b**) instability map at steady-state stress
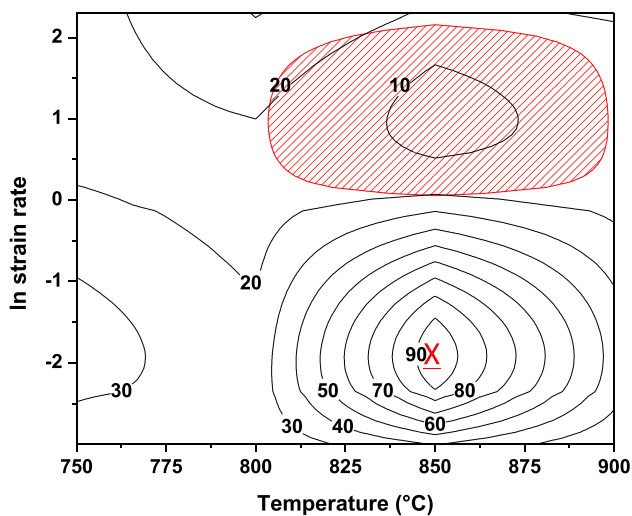
Fig. 9 Processing map of Ti-3.4Fe alloy at steady-state stress; the shaded area shows the instability region, and the region marked with X shows the optimum region to deform

images would show distinct grain boundaries that promote grain boundary sliding [44, 45]. These characteristics were not observed in the deformed microstructures of this alloy. However, since Fe has been reported to reduce the temperature of superplastic forming in other titanium alloys [43, 46, 47], the Fe content in the alloy may influence the microstructures, deformation temperatures and strain rates under which superplasticity may occur in this alloy. Hence, this is currently being investigated in our group.

The dynamic recovery observed in the steady-state stress processing map agrees with the observation that dynamic recovery is the dominant softening mechanism controlling hot deformation in the constitutive modelling and flow stress curves. Microstructural evidence of cracking was found in the unstable region predicted by the processing map. This is expanded on in Sect. 3.3.3. Further work would consider confirming superplasticity using hot tensile testing based on the parameters indicated on the processing map.

3.3.3 Microstructural validation

The microstructures of the samples at the stable and unstable regions were analysed using scanning electron microscopy. During hot deformation, energy is stored as dislocations, and this energy is released by dynamic recovery and recrystallisation, grain refinement, or grain growth [48]. The microstructures presented in Fig. 10 were taken at a total strain of 0.6 once deformation was completed. The images are of safe and unsafe regions of deformation of the Ti-3.4Fe alloy. Deformation at 850 °C and a strain rate of 0.05 s^{-1} and 0.1 s^{-1} were observed to be safe. This corroborates the observations made from the processing maps (Figs. 7 and 9).

Figure 10(a) shows a microstructure of the safe deformation region at conditions of 850 °C and 0.05 s^{-1}; the microstructure reveals observable rotated, kinked, and bent lamellar due to deformation under these parameters. These features are signatures that are attributed to dynamic recovery. For microstructure softened by dynamic recrystallisation, features like equiaxed or spheroidised grains are prominent [30]. These were not seen in the samples deformed under these conditions. This rules out the occurrence of dynamic recrystallisation as a possible deformation mechanism for this alloy under the tested conditions. One noticeable feature in Fig. 10(a) and (b) is the thinning of the lamellar, suggesting significant refinement of the lamellar structure in the deformed alloys compared to the as-cast microstructure (Fig. 1). This must have contributed to the higher power dissipation efficiency exhibited by the alloy at the optimum deformation conditions [49]. At regions of instability (shaded region in Fig. 9), 750 °C and 1 s^{-1} and 850 °C and 10 s^{-1} (Fig. 10(c) and (e)), cracks and inhomogeneity can be observed. The cracks can be viewed properly at higher magnification (Fig. 10(d)). These features validated the unsafe deformation region in Ti-3.4Fe alloy.

4 Conclusion

The hot deformation behaviour of the experimental Ti-3.4Fe alloy was analysed using constitutive modelling, processing mapping and the evolution of microstructures at the optimum deformation parameters and at the instability region after the deformation of the samples using the thermomechanical simulator, Gleeble® 3500. The constitutive constants, processing maps, flow stress curves, and the deformed microstructure led to the following conclusions:

a) The flow stress increased with increasing strain rate and decreasing temperature.
b) Ti-3.4Fe had an activation energy of 675 kJ.mol^{-1} at peak stress and 611 kJ.mol^{-1} at steady-state stress, with a stress exponent of 5.32 for peak stress and 4.91 for steady-state stress, suggesting a softening mechanism of dislocation climb and glide.
c) The Ti-3.4Fe processing maps had broad safe and smaller unsafe deformation regions. The optimum deformation parameters were found to be 850 °C at 0.1 s^{-1} for both peak stress and steady-state stress, and the unsafe deformation regions were found to be between 750 and 780 °C, and 810 and 890 °C at strain rates between 1 and 10 s^{-1} for peak stress and between 800 and 900 °C at strain rates between 1 and 10 s^{-1} for steady-state stress.
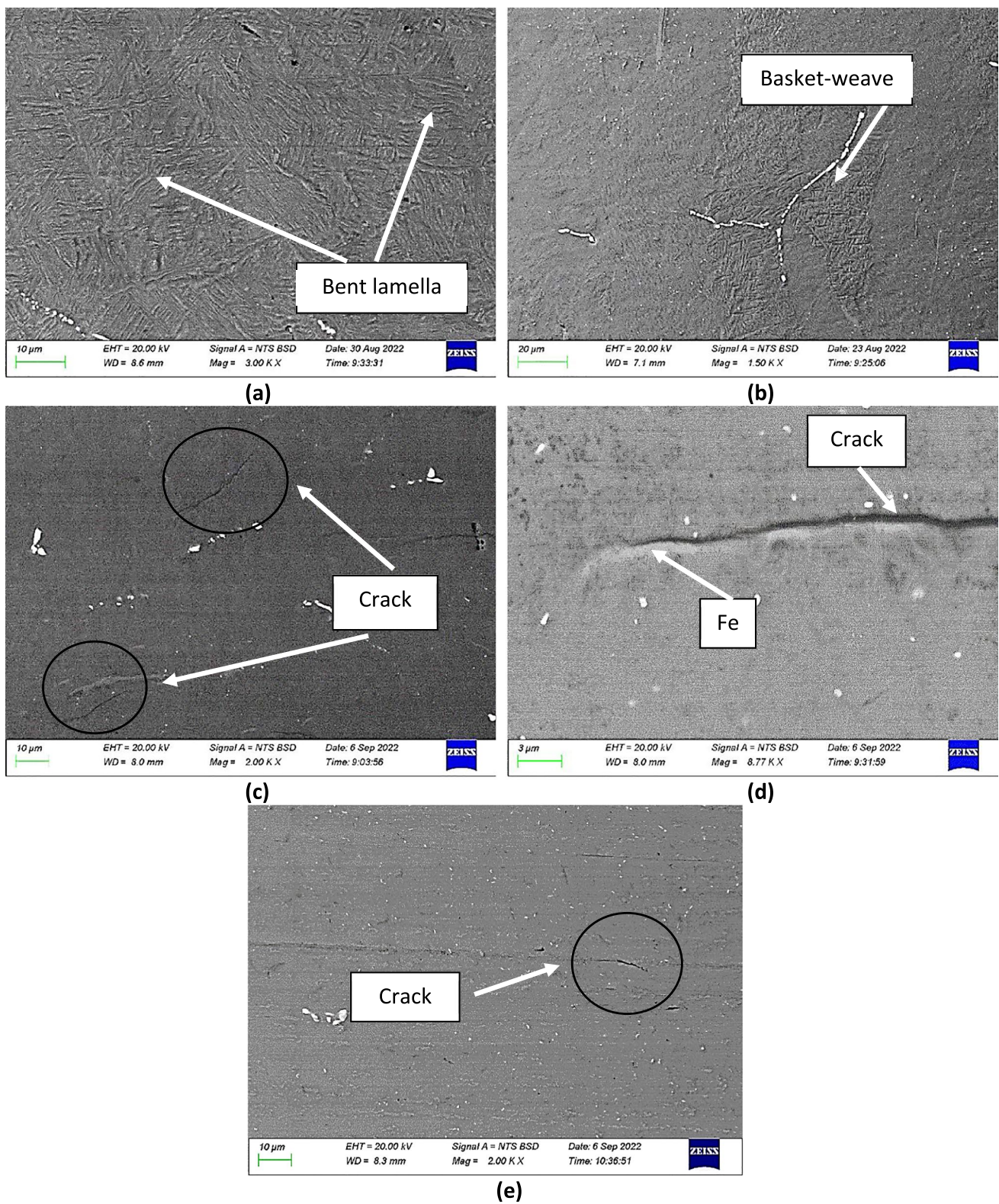d) Microstructural characterisation showed kinked, rotated and bent lamellar at the safe region (850 °C at 0.05 s^{-1})

Fig. 10 Microstructure at stable regions at (**a**) 850 °C at 0.05 s^{-1}, (**b**) 750 °C at 0.05 s^{-1}, and unstable regions at (**c**) 750 °C at 1 s^{-1}, (**d**) 750 °C at 1 s^{-1}, and (**e**) 850 °C at 10 s.$^{-1}$

controlled by dynamic recovery, as well as significant refinement of the lamellar structure.

e) The microstructure shows unsafe deformation in the form of cracks and inhomogeneity at 750 °C and 1 s^{-1}, and 850 °C and 10 s^{-1}.

Declarations

Competing interests The authors declare no competing interests.

References

1. Mahadule D, Khatirkar RK, Gupta SK, Gupta A, Dandekar TR (2022) Microstructure evolution and corrosion behaviour of a high Mo containing α + β titanium alloy for biomedical applications. J Alloys Compd 912:165240. https://doi.org/10.1016/j.jallcom.2022.165240

2. Bodunrin MO, Chown LH, van der Merwe JW, Alaneme KK (2020) Hot working behaviour of experimental Ti-4.5Al-1 V-3Fe alloy with initial lamellar microstructure. Int J Adv Manuf Technol 106:1901–1916. https://doi.org/10.1007/s00170-019-04718-7

3. Mosleh AO, Mikhaylovskaya AV, Kotov AD, Portnoy VK (2018) Arrhenius-type constitutive equation model of superplastic deformation behaviour of different titanium-based alloys. Defect Diffus Forum 385:45–52. https://doi.org/10.4028/www.scientific.net/DDF.385.45

4. Leyens C, Peters M (eds) (2003) Titanium and titanium alloys: fundamentals and applications. Wiley-VCH, Weinheim

5. Rack HJ, Qazi JI (2006) Titanium alloys for biomedical applications. Mater Sci Eng C 26:1269–1277. https://doi.org/10.1016/j.msec.2005.08.032

6. Okazaki Y, Rao S, Ito Y, Tateishi T (1998) Corrosion resistance, mechanical properties, corrosion fatigue strength and cytocompatibility of new Ti alloys without Al and V. Biomaterials 19(13):1197–1215. https://doi.org/10.1016/s0142-9612(97)00235-4

7. Trindade R, Albrektsson T, Tengvall P, Wennerberg A (2016) Foreign body reaction to biomaterials: on mechanisms for buildup and breakdown of osseointegration. Clin Implant Dent Relat Res 18(1):192–203. https://doi.org/10.1111/cid.12274

8. Dörner T, Haas J, Loddenkemper C, von Baehr V, Salama A (2006) Implant-related inflammatory arthritis. Nat Clin Pract Rheumatol 2:53–56. https://doi.org/10.1038/ncprheum0087

9. Esteban PG, Ruiz-Navas EM, Bolzoni L, Gordo E (2008) Low-cost titanium alloys? Iron may hold the answers. Met Powder Rep 63(4):24–27. https://doi.org/10.1016/S0026-0657(09)70040-2

10. Leshetla M, Klenam DE, van der Merwe J, Potgieter H, Whitefield D, Bodunrin MO (2022) Corrosion resistance of iron-containing experimental titanium alloys exposed to simulated body fluids. Mater Corros 73(8):1298–1307. https://doi.org/10.1002/maco.202213076

11. Bhola R, Kundu S, Mishra B, Olson DL (2011) Corrosion in titanium dental implants/prostheses - a review. Trends Biomater Artif Organs 25:34–46

12. Gao P, Zhan M, Fan X, Lei Z, Cai Y (2017) Hot deformation behavior and microstructure evolution of TA15 titanium alloy with nonuniform microstructure. Mater Sci Eng A 689:243–251. https://doi.org/10.1016/j.msea.2017.02.054

13. Wang K, Li MQ (2014) Flow behavior and deformation mechanism in the isothermal compression of the TC8 titanium alloy. Mater Sci Eng A 600:122–128. https://doi.org/10.1016/j.msea.2014.02.002

14. Zhao ZL, Li H, Fu MW, Guo HZ, Yao ZK (2014) Effect of the initial microstructure on the deformation behavior of Ti60 titanium alloy at high temperature processing. J Alloys Compd 617:525–533. https://doi.org/10.1016/j.jallcom.2014.08.092

15. Fu Q, Yuan W, Xiang W (2021) Dynamic softening mechanisms and microstructure evolution of TB18 titanium alloy during uniaxial hot deformation. Metals 11:789. https://doi.org/10.3390/met11050789

16. Prasad YVRK, Rao K, Sasidhara S (eds) (2015) Hot working guide: a compendium of processing maps, 2nd edn. ASM International, Ohio

17. He D, Yan X-T, Lin YC, Zhang S, Chen Z-J (2022) Microstructure evolution and constitutive model for a Ni-Mo-Cr base alloy in double-stages hot compression with step-strain rates. Mater Charact 194:112385. https://doi.org/10.1016/j.matchar.2022.112385

18. Shi S, Ge J, Lin YC, Zhang X, Zhou K (2022) High-temperature deformation behavior and recrystallization mechanism of a near beta titanium alloy Ti-55511 in β phase region. Mater Sci Eng A 847:7. https://doi.org/10.1016/j.msea.2022.143335

19. Bodunrin M, Obiko J, Klenam D (2023) On the uniaxial compression testing of metallic alloys at high strain rates: an assessment of DEFORM-3D simulation. Appl Sci 13(4):2686. https://doi.org/10.3390/app13042686

20. Jaspers SPFC, Dautzenberg JH (2002) Material behaviour in metal cutting: strains, strain rates and temperatures in chip formation. J Mater Process Technol 121:123–135. https://doi.org/10.1016/S0924-0136(01)01227-4

21. Bodunrin MO (2020) Flow stress prediction using hyperbolic-sine Arrhenius constants optimised by simple generalised reduced gradient refinement. J Mater Res Technol 9(2):2376–2386. https://doi.org/10.1016/j.jmrt.2019.12.070

22. Peng X, Guo H, Shi Z, Qin C, Zhao Z (2013) Constitutive equations for high temperature flow stress of TC4-DT alloy incorporating strain, strain rate and temperature. Mater Des 50:198–206. https://doi.org/10.1016/j.matdes.2013.03.009

23. Lin YC, Chen X-M (2011) A critical review of experimental results and constitutive descriptions for metals and alloys in hot working. Mater Des 32(4):1733–1759

24. Prasad YVRK, Seshacharyulu T (1998) Processing maps for hot working of titanium alloys. Mater Sci Eng A 243(1–2):82–88. https://doi.org/10.1016/S0921-5093(97)00782-X

25. Zhou G, Ding H, Cao F, Zhang B (2014) A comparative study of various flow instability criteria in processing map of superalloy GH4742. J Mater Sci Technol 30(3):217–222. https://doi.org/10.1016/j.jmst.2013.07.008

26. Bodunrin MO, Chown LH, van der Merwe JW, Alaneme KK (2020) On the substitution of vanadium with iron in Ti–6Al–4V: Thermo-Calc simulation and processing map considerations for design of low-cost alloys. Mater Sci Eng A 791:139622. https://doi.org/10.1016/j.msea.2020.139622

27. Nkhoma RKC, Siyasiya CW, Stumpf WE (2014) Hot workability of AISI 321 and AISI 304 austenitic stainless steels. J Alloys Compd 595:103–112. https://doi.org/10.1016/j.jallcom.2014.01.157

28. Satheesh Kumar SS, Raghu T, Bhattacharjee PP, Rao GA, Borah U (2015) Constitutive modeling for predicting peak stress characteristics during hot deformation of hot isostatically processed nickel-base superalloy. J Mater Sci 50:6444–6456. https://doi.org/10.1007/s10853-015-9200-0

29. Wang J, Wang K, Lu S, Li X, OuYang D, Qiu Q (2022) Softening mechanism and process parameters optimization of Ti-4.2Al-0.005B titanium alloy during hot deformation. J Mater Res Technol 17:1842–1851. https://doi.org/10.1016/j.jmrt.2022.01.128

30. Ning YQ, Luo X, Liang HQ, Guo HZ, Zhang JL, Tan K (2015) Competition between dynamic recovery and recrystallization during hot deformation for TC18 titanium alloy. Mater Sci Eng A 635:77–85. https://doi.org/10.1016/j.msea.2015.03.071

31. Park CH, Kim JH, Hyun Y-T, Yeom J-T, Reddy NS (2014) The origins of flow softening during high-temperature deformation of a Ti-6Al-4V alloy with a lamellar microstructure. J Alloys Compd 582:126–129. https://doi.org/10.1016/j.jallcom.2013.08.041

32. Mirzadeh H (2015) Simple physically-based constitutive equations for hot deformation of 2024 and 7075 aluminum alloys. Trans Nonferrous Met Soc China 25(6):1614–1618. https://doi.org/10.1016/S1003-6326(15)63765-7

33. Cabrera JM, Jonas JJ, Prado JM (1996) Flow behaviour of medium carbon microalloyed steel under hot working conditions. Mater Sci Technol 12(7):579–585. https://doi.org/10.1179/mst.1996.12.7.579

34. Souza PM, Sivaswamy G, Andreu A, Rahimi S (2022) A novel cyclic thermal treatment for enhanced globularisation kinetics in Ti-6Al-4V alloy: experimental, constitutive and FE based analyses. J Alloys Compd 898:162859. https://doi.org/10.1016/j.jallcom.2021.162859

35. Frost HJ, Ashby MF (1982) Deformation-mechanism maps: the plasticity and creep of metals and ceramics. Franklin Book Company, Incorporated, New Jersey

36. McQueen HJ, Ryan ND (2002) Constitutive analysis in hot working. Mater Sci Eng A 322(1–2):43–63. https://doi.org/10.1016/S0921-5093(01)01117-0

37. Maia A, Ferreira E, Oliveira MC, Menezes LF (2017) Numerical optimization strategies for springback compensation in sheet metal forming. In: Davim JP (ed) Computational methods and production engineering. Woodhead Publishing, Cambridge, pp 51–82

38. Lakshmi AA, Srinivasa Rao Ch, Gangadhar J, Srinivasu Ch, Singh SK (2017) Review of processing maps and development of qualitative processing maps. Mater Today: Proc 4(A):846–956

39. Opěla P, Schindler I, Kawulok P, Kawulok R, Rusz S, Navrátil H, Jurča R (2020) Correlation among the power dissipation efficiency, flow stress course, and activation energy evolution in Cr-Mo low-alloyed steel. Materials 13(16):3480. https://doi.org/10.3390/ma13163480

40. Prasad YVRK, Ravichandran N (1991) Effect of stacking fault energy on the dynamic recrystallization during hot working of FCC metals: a study using processing maps. Bull Mater Sci 14:1241–1248. https://doi.org/10.1007/BF02744618

41. Guo Z, Miodownik AP, Saunders N, Schillé J-P (2006) Influence of stacking-fault energy on high temperature creep of alpha titanium alloys. Scr Mater 54(12):2175–2178. https://doi.org/10.1016/j.scriptamat.2006.02.036

42. Ouyang D, Wang K-l, Cui X (2012) Dynamic recrystallization of Ti–6Al–2Zr–1Mo–1V in β forging process. Trans Nonferrous Met Soc China 22(4):761–767. https://doi.org/10.1016/S1003-6326(11)61242-9

43. Kotov AD, Postnikova MN, Mosleh AO, Mikhaylovskaya AV (2022) Influence of Fe on the microstructure, superplasticity and room-temperature mechanical properties of Ti–4Al–3Mo–1V-0.1B alloy. Mater Sci Eng A 845:143245. https://doi.org/10.1016/j.msea.2022.143245

44. Kim JH, Chang YW, Lee CS, Kwon Ha T (2003) High-temperature deformation behavior of a gamma TiAl alloy—microstructural evolution and mechanisms. Metall Mater Trans A 34:2165–2176. https://doi.org/10.1007/s11661-003-0280-0

45. Sieniawski J, Motyka M (2007) Superplasticity in titanium alloys. J Achiev Mater Manuf Eng 24:123–130

46. Koike J, Shimoyama Y, Ohnuma I, Okamura T, Kainuma R, Ishida K, Maruyama K (2000) Stress-induced phase transformation during superplastic deformation in two-phase Ti–Al–Fe alloy. Acta Mater 48(9):2059–2069. https://doi.org/10.1016/S1359-6454(00)00049-5

47. Masuda H, Sato E (2020) Diffusional and dislocation accommodation mechanisms in superplastic materials. Acta Mater 197:235–252

48. Sommitsch C, Radis R, Krumphals A (2012) Microstructure control in processing nickel, titanium and other specila alloys. In: Lin J, Balint DS, Pietrzyk M (eds) Microstructure evolution in metal forming processes. Woodhead Publishing, Cambridge, pp 337–383

49. Zhang W, Liu H, Ding H, Fujii H (2019) Grain refinement and superplastic flow in friction stir processed Ti–15V–3Cr–3Sn–3Al alloy. J Alloys Compd 803:901–911. https://doi.org/10.1016/j.jallcom.2019.06.323

Publisher's note Springer Nature remains neutral with regard to jurisdictional claims in published maps and institutional affiliations.